

PAPER • OPEN ACCESS

## Revealing capacity fading in Sb-based anodes using symmetric sodium-ion cells

To cite this article: Yonas Tesfamhret *et al* 2021 *J. Phys. Mater.* 4 024007

View the [article online](#) for updates and enhancements.



**240th ECS Meeting** ORLANDO, FL

Orange County Convention Center Oct 10-14, 2021



Abstract submission due: April 9

**SUBMIT NOW**



## PAPER

## OPEN ACCESS

## RECEIVED

30 November 2020

## REVISED

22 February 2021

## ACCEPTED FOR PUBLICATION

4 March 2021

## PUBLISHED

25 March 2021

Original content from this work may be used under the terms of the [Creative Commons Attribution 4.0 licence](#).

Any further distribution of this work must maintain attribution to the author(s) and the title of the work, journal citation and DOI.



# Revealing capacity fading in Sb-based anodes using symmetric sodium-ion cells

Yonas Tesfamhret, Marco Carboni, Habtom Desta Asfaw , Jolla Kullgren and Reza Younesi\*

Department of Chemistry-The Ångström Laboratory, Uppsala University, Uppsala 75121, Sweden

\* Author to whom any correspondence should be addressed.

E-mail: [reza.younesi@kemi.uu.se](mailto:reza.younesi@kemi.uu.se)**Keywords:** antimony, graphite, interphase, sodium-ion battery, capacity fading, symmetric cells

## Abstract

The electrochemical performance of negative active materials employed in sodium-ion batteries is dependent on the amount of  $\text{Na}^+$  available in the test cells. As such, electrodes that exhibit long cycle-life and high coulombic efficiency (CE) in half-cells could suffer from fast capacity fading in full-cells as a result of unstable solid electrolyte interphase (SEI) and mechanical degradation leading to loss of active materials. In this work, the performance of Sb-graphite composite active materials prepared by extended ball-milling was evaluated in sodium half-cells and various types of symmetric cells (SCs). In half-cell tests, the composite electrodes provided specific capacities in the range 350–600 mAh  $\text{g}^{-1}$  at C/20 with initial CE of 82%. A stable capacity of 380 mAh  $\text{g}^{-1}$  was observed in the subsequent 100 cycles with the CE increasing to nearly 99%. However, self-discharge tests on half-cells and galvanostatic cycling of SCs revealed poor capacity retention as a result of parasitic reaction occurring through the SEI layer. Contrary to half-cells, the SCs revealed that Sb electrodes suffered from sharp capacity losses when a limited amount of  $\text{Na}^+$  ions was available in the cells. This is also characteristic of full-cells in which the sodium ions are supplied by the positive electrode.

## 1. Introduction

The development of sodium-ion batteries (SIBs) with practical anode and cathode materials which offer high energy density and long cycle life has been a major challenge to their use in commercial applications [1]. Graphite and silicon, which are the most common intercalation and alloying anode materials for lithium-ion batteries (LIBs), exhibit limited  $\text{Na}^+$  storage capacity [2, 3]. Hard carbons are considered as the ‘standard’ anode materials for SIBs, but usually have capacities limited to up to 300 mAh  $\text{g}^{-1}$  [4–6]. A number of sodium alloys with Sb, Ge, and Sn have been proposed in an effort to increase the capacity of negative electrode materials in SIBs [7–13]. Among these, Sb possesses promising characteristics such as high theoretical capacity of 660 mAh  $\text{g}^{-1}$  and an average voltage of 0.6 V vs.  $\text{Na}^+/\text{Na}$  [7, 8]. However, a drastic volume increase ( $\sim 390\%$ ) upon alloying with Na presents a major challenge to practical applications [7, 8]. To prevent performance degradation during cycling as a result of volume variations, mainly two approaches have been proposed: a) reducing Sb particle size and b) introducing carbon additives to prepare Sb/C composite electrodes with the ability to accommodate mechanical stress [14–19]. Previous reports have demonstrated that embedding Sb particles in carbon matrices led to considerable improvement in reversibility and cycle life of the electrodes [14–17]. For instance, Zhu *et al* [14] demonstrated that a reversible specific capacity of 640 mAh  $\text{g}^{-1}$  could be achieved when Sb nanoparticles were mixed with carbon nanofibers via electrospinning process. Enhancement of performance was reported by Li *et al* [15] for a Sb–C–graphene fibrous electrodes. A Sb/C composite anode synthesized by mechanical ball milling of Sb powder with SuperP<sup>®</sup> carbon was also demonstrated to offer a reversible specific capacity of 610 mAh  $\text{g}^{-1}$  with capacity retention of 94% over 100 cycles [16].

Most studies are based on half-cells in which the sodium metal counter electrode supplies an excess amount of  $\text{Na}^+$  to sustain cell operation over extended cycles. As long as sufficient amount of electrolyte is

used, little or no capacity fading is normally observed, even if parasitic reactions are consuming sodium ions in the cell. The true cycle life of active materials can only be studied under conditions in which limited amounts of sodium ions are supplied by the positive electrodes. Several works have shown the advantages of symmetric cells (SCs) in unravelling the true behaviour of electrode materials. Dahn *et al* [20] proposed the use of SCs to assess the impact of electrolyte additives and new electrode materials on cell performance. Similarly, Lee *et al* [21] investigated influence of LiFSI electrolyte salt on performance of graphite electrodes using SCs for LIBs. In addition, it is worth noting that considerable increases in the resistance of Na metal electrode makes it difficult to assess the rate capability of alloys and other negative active materials using half-cell designs [22]. Also, the cross-talk between Na metal electrode and the working can influence the results [23]. Thus, SCs are considered useful in the evaluation of the impact of electrolyte salts, solvents, and additives on the cycling performance of electrodes (CE, cycle life and rate capability) in SIBs.

In this article, antimony–graphite (Sb–graphite) composite materials were prepared by ball-milling Sb with graphite over 48 h. Sb was selected since it is widely documented as a stable alloying anode material for SIBs, based on half-cells. For material preparation, a simple and reproducible ball-milling method was employed. Different prototype SCs containing as-prepared and pre-sodiated electrodes were investigated in addition to half-cells to explain capacity fading arising from loss of sodium ions to irreversible reactions.

## 2. Materials and methods

### 2.1. Electrode fabrication

The composite electrode (Sb–graphite) was obtained by first mixing Sb powder (Strem Chemicals®, 99.8%) and N-methyl-2-pyrrolidone (NMP, Sigma-Aldrich®, 99.9%) with a 1:2 weight ratio. The resulting slurry was ball-milled in a PM100 (Retsch®) for 48 h at 400 rpm with rest intervals of 2 min every 5 min to decrease the particle size of the Sb powder. NMP was selected as a solvent to avoid potential oxidation of Sb in the process. The mixture was then washed with acetone four times in a spin-dryer and dried at 80 °C for 12 h in a vacuum oven to remove NMP and acetone. The Sb powder was then mixed with commercial graphite (Alfa Aesar®, 200-mesh) in 3:2 wt ratio, and ball milled again for 12 h at 300 rpm. Afterwards, the composite active material antimony–graphite (Sb–graphite), sodium alginate (Na–Alg, Sigma-Aldrich®) and carbon black (C65®) were mixed with 85:10:5 wt% ratio, respectively. The resulting powder was mixed with water in 4:1 wt% ratio, respectively, and further milled and blended in a planetary ball-miller (Retsch® PM4). The slurry was coated onto aluminium foil using a bar-coater and dried at ambient conditions. Then, 13 mm diameter disks were punched out of the coating to prepare electrodes for electrochemical tests. In addition, control electrodes composed of only as-received graphite (pristine graphite) and ball-milled graphite were prepared following the same procedure. Before use in electrochemical cells, the electrodes were dried at 120 °C in a vacuum oven for about 12 h and stored in an Ar-filled glovebox. The mass loadings on Sb–graphite, pristine graphite and ball-milled graphite were, respectively,  $3.5 \pm 0.3 \text{ mg cm}^{-2}$ ,  $2 \pm 0.3 \text{ mg cm}^{-2}$  and  $3 \pm 0.5 \text{ mg cm}^{-2}$ .

### 2.2. Morphology and structure characterization

Scanning electron microscopy (SEM) images and electron dispersive x-ray spectroscopy (EDX) maps were taken using Zeiss/LEO 1550 at 10 kV accelerating voltage. The Raman spectra were recorded using Renishaw inVia Raman Microscope by illuminating the samples with a 50 mW, 532 nm laser source operated at 0.5% power and focused using a 50× objective lens. Each measurement involved a 20 s laser exposure and 20 accumulations. Peak-fitting was done using pseudo-voigt functions. X-ray powder diffraction (XRD) experiment was performed using a Siemens® D5000 diffractometer (45 kV, 40 mA) with Cu–K $\alpha$  radiation in Bragg-Brentano mode and zero-background Si sample holders. The data was collected between 10°–90° ( $2\theta$ ) with a step size and time per step of 0.02° and 1.5 s, respectively. X-ray photoelectron spectroscopy (XPS) analysis was performed on Sb/graphite electrodes cycled in half-cell setup. The electrodes were rinsed with DMC in an Ar-filled glovebox, followed by inert transfer for the measurement. Pristine and Sb/graphite composite electrode soaked for 24 h were also prepared in the same manner. Samples were analyzed using a Phi-5500 instrument with monochromatized Al K $\alpha$  radiation (1486.6 eV). The obtained spectra were calibrated with respect to the hydrocarbon peak set to 284.4 eV.

### 2.3. Cell assembly and electrochemical testing

The electrolyte used for electrochemical testing was 1 M NaPF<sub>6</sub> in a 1:1 volume ratio of ethylene carbonate (EC, BASF) and diethylene carbonate (DEC, BASF) with a 5 vol.% fluoroethylene carbonate (FEC, Sigma-Aldrich®, 99.9%) as an additive. The NaPF<sub>6</sub> salt (Sigma-Aldrich®, 98%) was dried at 70 °C for 48 h prior to electrolyte preparation. For electrochemical tests, two-electrode half-cells and SCs were assembled in pouch-cell designs using Sb–graphite, pristine graphite and ball-milled graphite as working electrodes, and

Na metal ( $\phi = 16$  mm) disks as combined counter and reference electrodes with electrolyte-soaked glass fiber separators (Whatman®, diameter = 20 mm) in between. Approximately 100  $\mu\text{l}$  of electrolyte was used in each cell. The electrolyte preparation and cell assembly were performed in an Ar-filled glove box with  $\text{O}_2$  and  $\text{H}_2\text{O}$  level below 3 ppm. After the Sb–graphite electrodes are sodiated/de-sodiated in half cell setup, the cells were carefully disassembled in the Ar-filled glovebox and the cycled Sb–graphite electrode was recovered. A new SC containing the recovered electrode was then assembled with 100  $\mu\text{l}$  fresh 1 M  $\text{NaPF}_6$  EC:DEC (containing 5 vol% FEC) electrolyte. Different types of SCs designated as SC-1, SC-2 and SC-3 were assembled. The SC-1 cell consisted of a fully sodiated Sb–graphite electrode and a pristine Sb–graphite electrode. In the SC-2 cell, the working Sb–graphite electrode was cycled six times and then fully sodiated prior to cell-assembly, while the counter Sb–graphite electrode was as-prepared. Both the working (sodiated) and counter (de-sodiated) Sb–graphite electrodes were cycled at least six times before assembling to make the SC-3 cell. The specific capacity for the SCs is calculated based on the electrode with the lower mass. The electrodes had similar mass loading, only differing by several percentage units.

Cycling voltammetry (CV) measurements were carried out using Bio-Logic® MPG2-1 potentiostat at a scan rate of 0.1  $\text{mV s}^{-1}$  in the voltage range from 0.02 to 2.00 V vs.  $\text{Na}^+/\text{Na}$ . Measured currents were normalized to the total mass of the active materials. Galvanostatic experiments were performed using LANDT® battery testing system at specific currents of 15, 30, 60 and 300  $\text{mA g}^{-1}$  (C/20, C/10, C/5 and 1C respectively) in a voltage range from 0.02 to 2.00 V vs.  $\text{Na}^+/\text{Na}$ . A specific current of 30  $\text{mA g}^{-1}$  was applied for the galvanostatic cycling of SCs, between voltage limits of  $\pm 1.2$  V (for SC-1 and SC-2) and  $\pm 0.7$  V (for SC-3).

### 3. Results and discussion

#### 3.1. Morphological and structural changes caused by prolonged ball-milling

Potential changes in the particle morphology and crystallinity caused by ball-milling were studied before electrochemical characterizations. As shown in the SEM images in figures 1(a) and (b), the graphite flakes measured below 75  $\mu\text{m}$  in lateral size before milling and decreased to below 30  $\mu\text{m}$  after a 12 h ball-milling. The SEM images in figures 1(c) and (d) of the ball-milled Sb–graphite composite electrode (Sb–graphite) showed that the Sb particles underwent significant reduction in size after milling and were dispersed in a matrix graphite flakes. Inspection of the back-scattered SEM images in figure 1(d) revealed that the Sb particles decreased from 44  $\mu\text{m}$  (as-received) to less than 2  $\mu\text{m}$  after ball-milling. Therefore, the ball-milling process was successful in forming a good dispersion of Sb particles in a graphitic matrix, as also shown in the EDX elemental maps of Sb, C and O in figures 1(e)–(g), to form composite electrodes with higher specific surface area and better ability to buffer volume changes during cycling.

Apart from morphological changes, ball-milling can affect the long-range ordering in graphite [24, 25] and antimony crystallites. The XRD patterns acquired for pristine graphite, ball-milled graphite, pristine Sb, ball-milled Sb, and ball-milled Sb–graphite composite materials are presented in figure 2(a). The (002) graphitic peak significantly broadened after 12 h ball milling indicating the decrease in its crystallinity as the result of increasing defects. Similarly, the diffraction peaks of Sb become broader with lower intensity after ball milling. The XRD patterns also confirmed the purity of the Sb phase, and that no crystalline oxide phase was observed either before or after milling. Furthermore, the Raman spectra of the ball-milled and pristine graphite powder (see figure 2(e), and note that intensity has been normalized to unity) showed the characteristic D-, G- and 2D-bands of graphite at positions of around 1350, 1580 and 2720  $\text{cm}^{-1}$ , respectively [26–28]. The D band in the spectrum of pristine graphite electrode was less intense, while the more dominant G band was much sharper due to the absence of defects in the crystal structure. The  $I_D/I_G$  intensity ratio and the full-width at half-maximum of the bands increased after ball-milling as defects such as exfoliation, interlayer expansion and size reduction disrupted the long-range graphitic order. Such structural changes caused an increase in Raman scattering contributions from defects [29, 30], particularly in the case of ball-milled graphite in which the D and D' bands increased considerably.

#### 3.2. Electrochemical performance of Sb/graphite composite electrodes

As shown in the CVs in figure 3(a), the first reduction scan in Sb–graphite anode showed mainly one broad peak around 0.28 V due to amorphization of crystalline Sb and nucleation of crystalline sodium-antimony alloy phases [31, 32]. From the second cycle onwards, two more cathodic peaks were observed at 0.5 V and 0.65 V originating from the multi-step alloying of Sb with Na to form the amorphous  $\text{Na}_x\text{Sb}$  (for  $x > 1.5$ ) phase and the crystalline hexagonal  $\text{Na}_3\text{Sb}$  phase upon full sodiation [33, 34]. As reported previously, the dealloying process during charge resulted in largely amorphous Sb and only a single CV peak could be observed around 0.8 V. To assess the capacity contribution of the graphite component, CV test was performed on the ball-milled graphite electrode (the dotted-curve CV in figure 3(a)) as well, which showed a

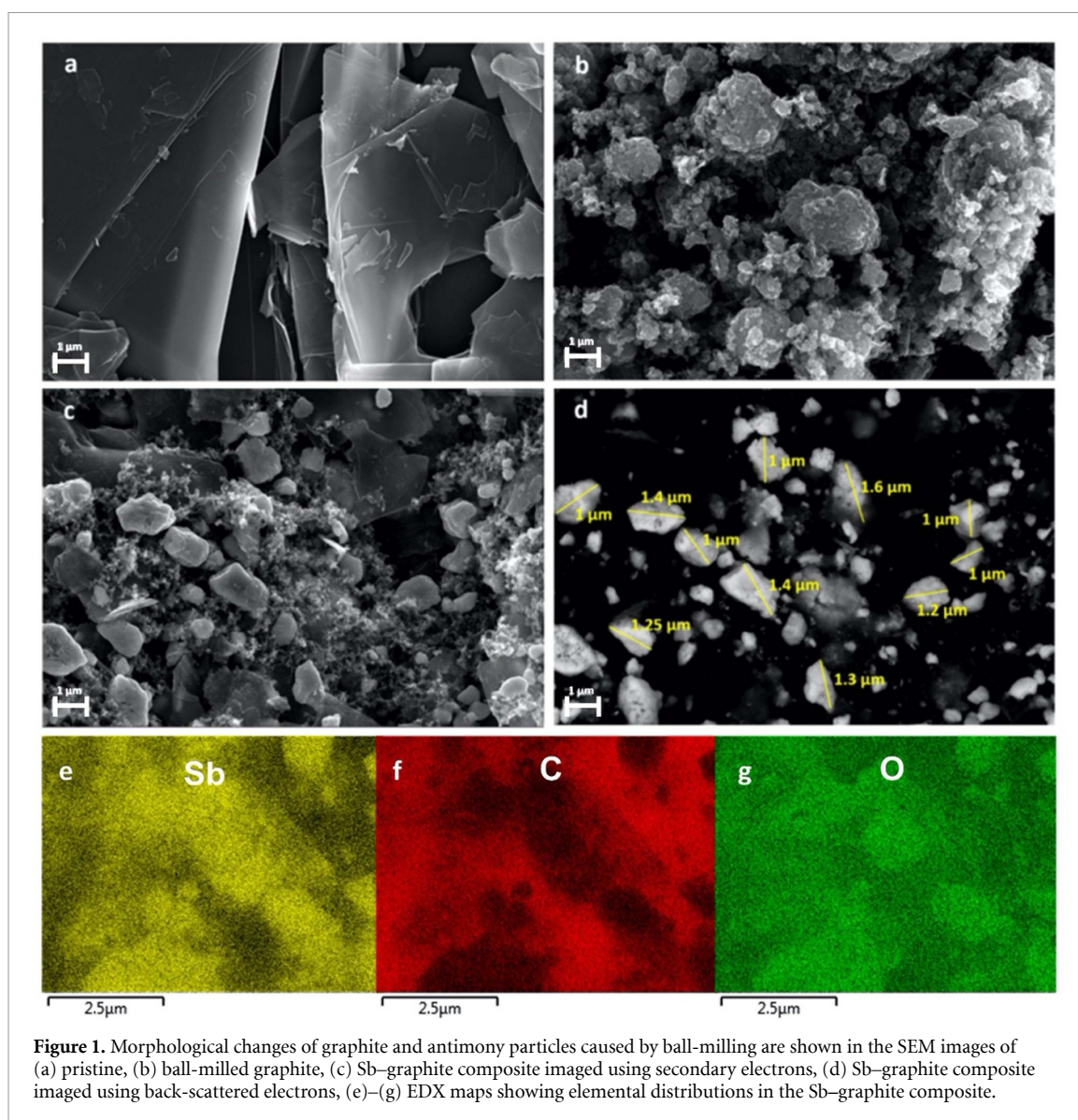


**Figure 1.** Morphological changes of graphite and antimony particles caused by ball-milling are shown in the SEM images of (a) pristine, (b) ball-milled graphite, (c) Sb-graphite composite imaged using secondary electrons, (d) Sb-graphite composite imaged using back-scattered electrons, (e)–(g) EDX maps showing elemental distributions in the Sb-graphite composite.

large peak below 0.5 V during first discharge due to electrolyte decomposition resulting in surface passivation. Largely capacitive behaviour was observed in the following cycles with a maximum current of  $0.05 \text{ A g}^{-1}$  as opposed to nearly  $1 \text{ A g}^{-1}$  for the composite electrodes. A typical galvanostatic discharge-charge curves of Na-Sb alloying electrodes are shown in figure 3(b). Most of the electrode reactions occur within the range 0.3–0.9 V, as widely reported in the literature [35]. The comparisons of the  $\text{Na}^+$  storage capacities of crystalline graphite, ball-milled graphite and ball-milled Sb-graphite composite electrodes are provided in figure 3(c) along with the respective CEs in figure 3(d). All three materials were galvanostatically cycled using at  $30 \text{ mA g}^{-1}$ .

The pristine graphite electrode exhibited poor electrochemical activity with only  $2 \text{ mAh g}^{-1}$  maintained over subsequent cycles, after first cycle. On the contrary, the ball-milled graphite provided reversible capacity of about  $125 \text{ mAh g}^{-1}$  for the second cycle which decreased and stabilized to about  $90 \text{ mAh g}^{-1}$  after 100 cycles. The Sb-graphite composite provided a specific discharge capacity of  $450 \text{ mAh g}^{-1}$  with a CE of 85% for the first cycle, and then a reversible capacity of about  $380 \text{ mAh g}^{-1}$  in the subsequent cycles. If normalized to the mass of Sb in the composite, which was approximately 60 wt.%, and subtracting the capacity contribution due to graphite ( $125 \text{ mAh g}^{-1}$ ), the specific capacity would be  $600 \text{ mAh g}^{-1}$ , which was very close to the theoretical capacity of Sb ( $660 \text{ mAh g}^{-1}$ ). It should also be noted that capacity due to graphite in the composite could be overestimated since it was structurally different from the graphite ball-milled separately, as observed in the Raman spectra provided in figures 1(b)–(e). The electrochemical performance of Sb-graphite at different C-rates are shown in figures (c) and (d). At C/20 rate, the specific capacity was nearly  $400 \text{ mAh g}^{-1}$  over 40 cycles. Increasing the rate to C/10 and C/5 decreased the stable capacity only slightly to approximately  $390$  and  $360 \text{ mAh g}^{-1}$ , respectively. In general, it can be concluded that the specific

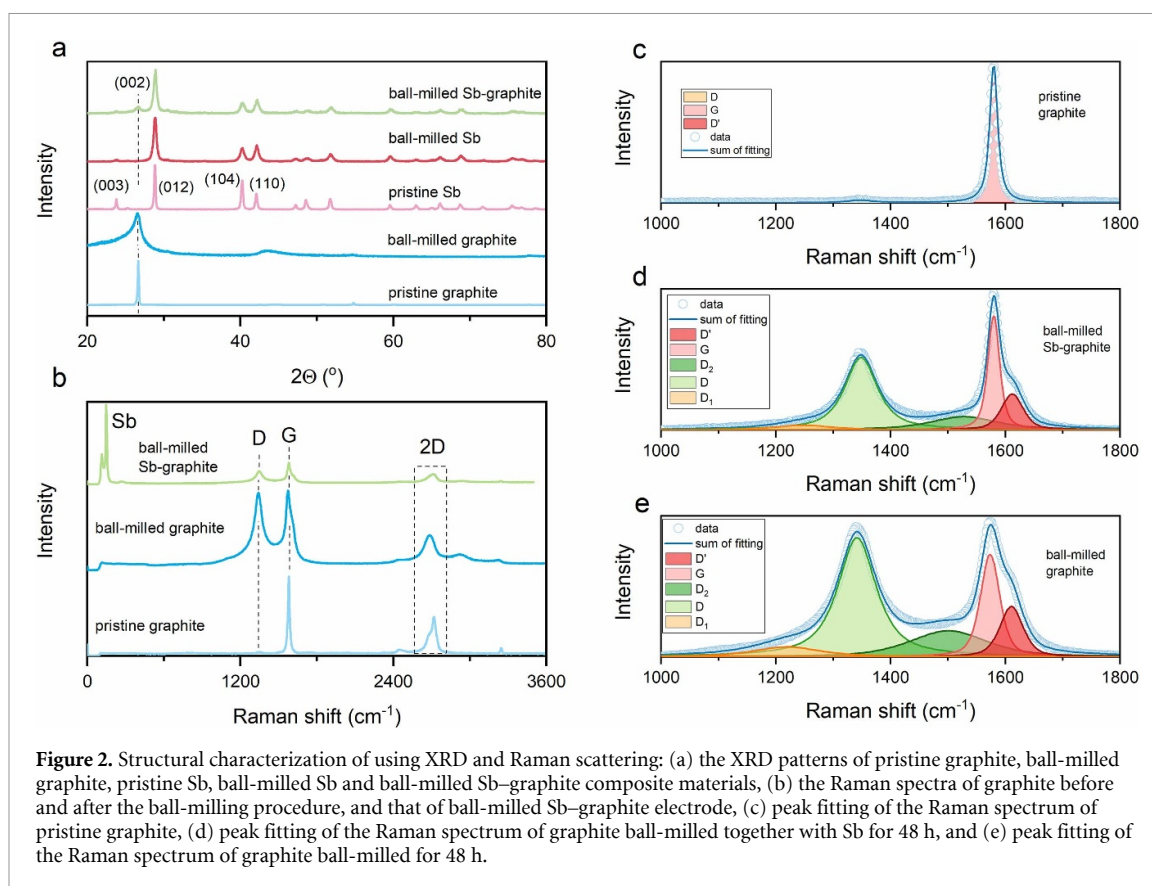
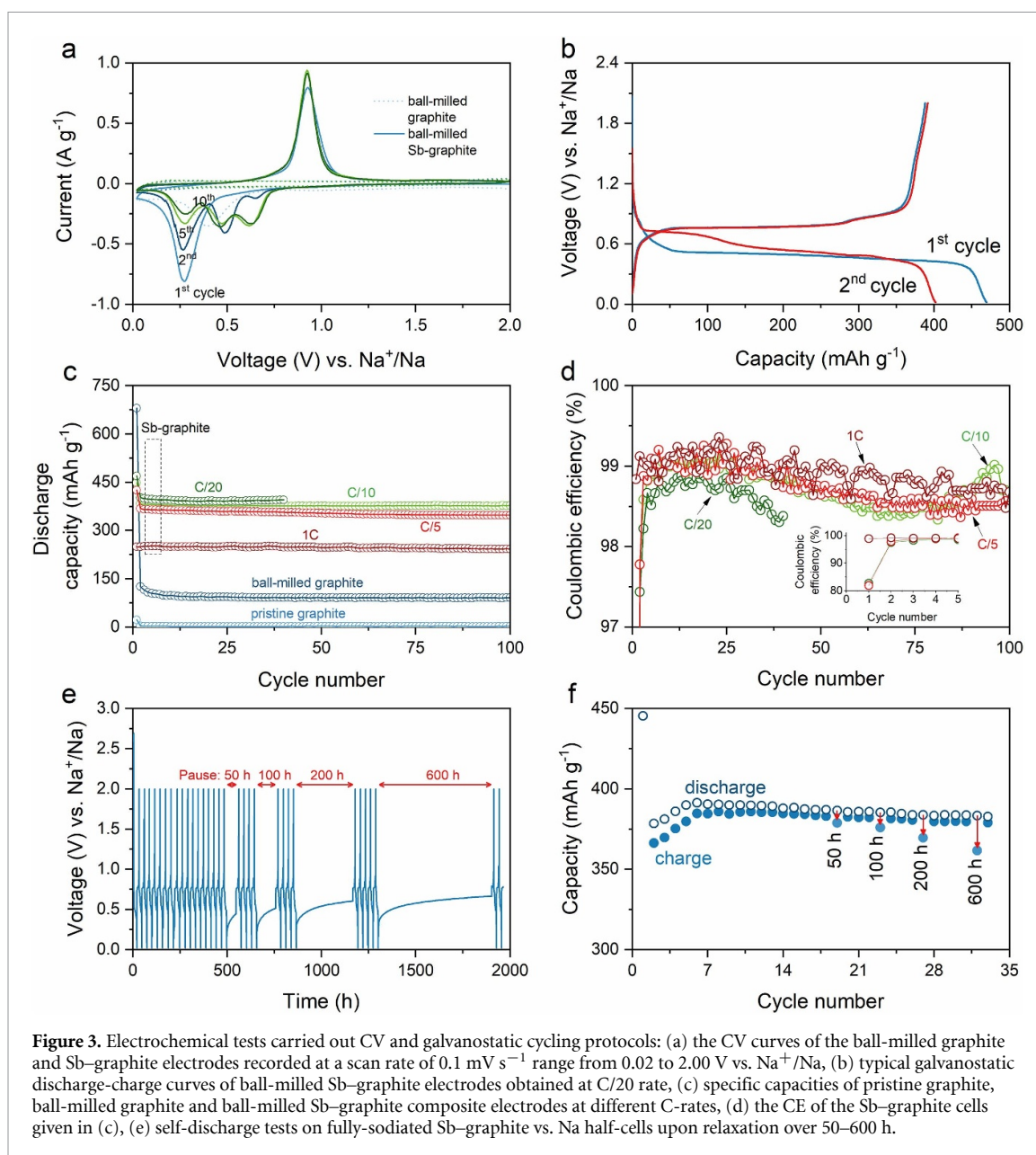


**Table 1.** Comparison of the electrochemical performance of Sb-based anode in our work with that of some previously published Sb-based anode performance for SIBs. Note that the studies included reserve some type of similarity to ours, whether it be electrode preparation method, electrode composition etc.

| References            | Electrode composition weight ratio (wt.%)               | Mass loading ( $\text{mg cm}^{-2}$ ) | Capacity (at specific current $\text{mA g}^{-1}$ )   | Capacity retention (cycle life) |
|-----------------------|---|--------------------------------------|--|---------------------------------|
| Our work              | BM <sup>1</sup> Sb/graphite/CB/Na-Alg 51/34/5/10 wt.%   | $3 \pm 0.5$                          | $550 \text{ mAh g}^{-1}_{\text{Sb}}$ or $375 \text{ mAh g}^{-1}_{\text{am}}$ <sup>3</sup> ( $60 \text{ mA g}^{-1}$ ) | >95% retention (>100 cycles)    |
| Our work              | BM Sb/graphite/CB/Na-Alg 51/34/5/10 wt.%                | $3 \pm 0.5$                          | $595 \text{ mAh g}^{-1}_{\text{Sb}}$ or $395 \text{ mAh g}^{-1}_{\text{am}}$ ( $15 \text{ mA g}^{-1}$ )              | >98% retention (>30 cycles)     |
| Lee et al [17]        | BM Sb/graphite/CB/Na-Alg 51/34/5/10 wt.%                | 1.5                                  | $310 \text{ mAh g}^{-1}_{\text{am}}$ ( $30 \text{ mA g}^{-1}$ )  | ~100% retention (160 cycles)    |
| Yang et al [16]       | 10 nm Sb/CB/CMC 56/34/10 wt.%                           | 3.3                                  | $610 \text{ mAh g}^{-1}_{\text{Sb}}$ ( $36 \text{ mA g}^{-1}$ )  | >90% retention (100 cycles)     |
| Wang et al [14]       | Electrospun Sb NP <sup>2</sup> /carbon fiber 54/46 wt.% | 3                                    | $320 \text{ mAh g}^{-1}_{\text{am}}$ (At $30 \text{ mA g}^{-1}$ )  | >80% retention (300 cycles)     |
| Monconduit et al [35] | BM Sb particle/CB+carbon fiber/CMC 70/15/15 wt.%        | 1.4                                  | $576 \text{ mAh g}^{-1}_{\text{Sb}}$ ( $15 \text{ mA g}^{-1}$ )  | >90% retention (200 cycles)     |
| Liu et al [36]        | SnSb/carbon nanofiber/CB/CMC 48/32/10/10 wt.%           | 1.5-2                                | $392 \text{ mAh g}^{-1}_{\text{am}}$ ( $30 \text{ mA g}^{-1}$ )  | ~100% retention (200 cycles)    |
| Cao et al [19]        | Sb/MWCNT <sup>4</sup> /Super P 80/10/10 wt.%            | 1.6                                  | $552 \text{ mA g}^{-1}$ ( $800 \text{ mA g}^{-1}$ )  | ~94.3% retention (>300 cycles)  |

1. BM = ball milled, 2. NP = nano particle, 3. am = active material, 4. MWCNT = multiwalled carbon nanotubes

capacities of the electrodes at C/20 to C/5 rates were in the range from 350 to 400  $\text{mAh g}^{-1}$ . However, a significant capacity loss was observed at higher C-rates, with the specific capacity being 250  $\text{mAh g}^{-1}$  at 1C. The associated CE of the half-cells were approximately 80% at C/20, C/10, and C/5, and 75% at 1C. In the subsequent cycles, the CE for all C-rates increased to roughly 99% and stable capacities were obtained



over 100 cycles with little or no fading, as it is typically reported for Sb-based electrodes tested in half-cells. The measured capacities are comparable with capacities reported in other studies (see table 1).

### 3.3. Stability of the solid electrolyte interphase (SEI) layer and capacity fading in Sb-graphite composite electrodes

The nature and dynamics of the SEI layer on the negative electrodes in SIBs electrolytes are not well-understood [37], but it is suspected that the SEI could be unstable during charge-discharge cycles leading to aggravated self-discharge and capacity fading [38]. To evaluate the stability of the SEI layer, and the extent of self-discharge, Sb-graphite electrodes were allowed to relax at OCV over extended periods after galvanostatic discharge to 0.02 V, i.e. in their fully sodiated states while connected to battery testing system, as shown in figures 3(e) and (f). The self-discharge observed during the OCV relaxation resulted in capacity loss which increased with increasing time of relaxation. As can be observed in figure 3(f), a 6% capacity loss was recorded for the longest pause (600 h), while the voltage relaxed to around 0.5 V.

The SEI formation on the Sb/graphite composite electrode was analysed by XPS after 5 and 50 cycles at sodiated and desodiated states which were compared to pristine and soaked samples (figure 4). The sodiated state corresponded to an electrode cycled up to end of discharge (0.02 V) and desodiated state corresponds to an electrode cycled to the end of charge (2 V).

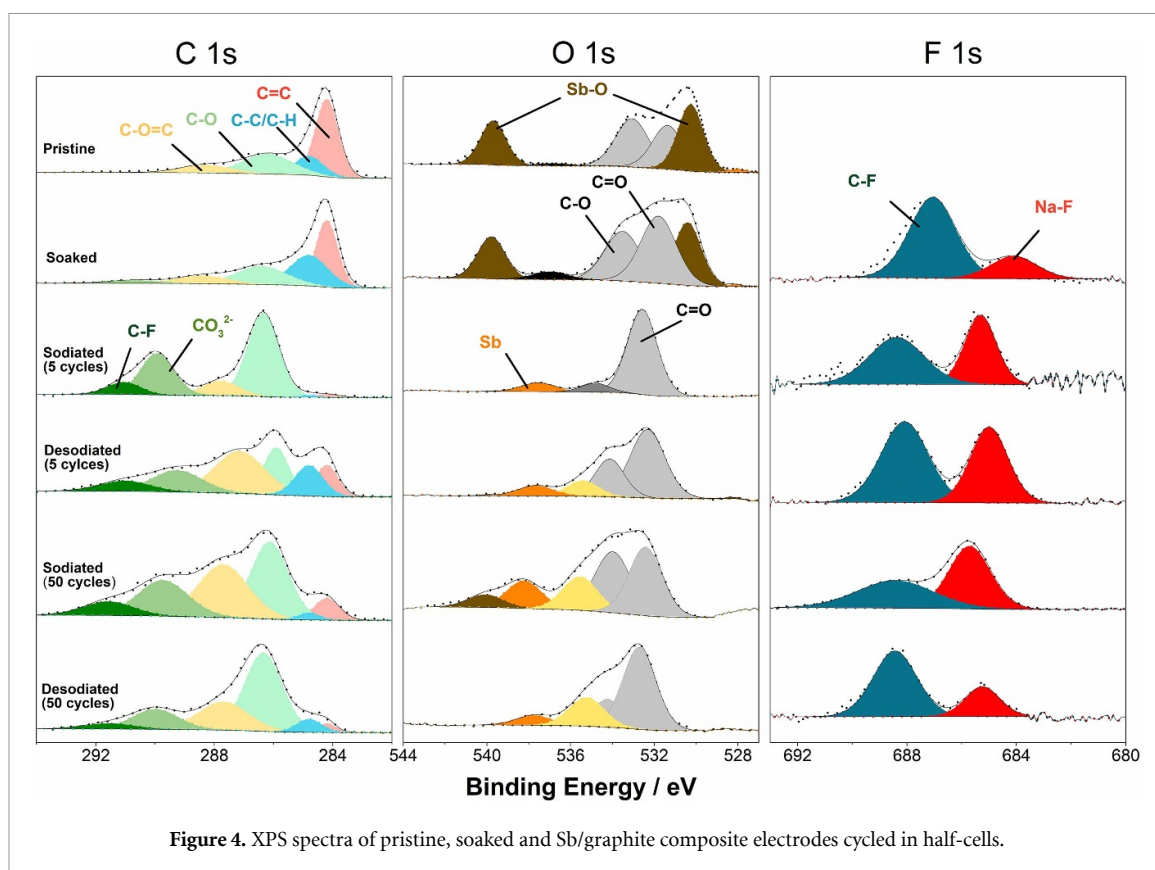


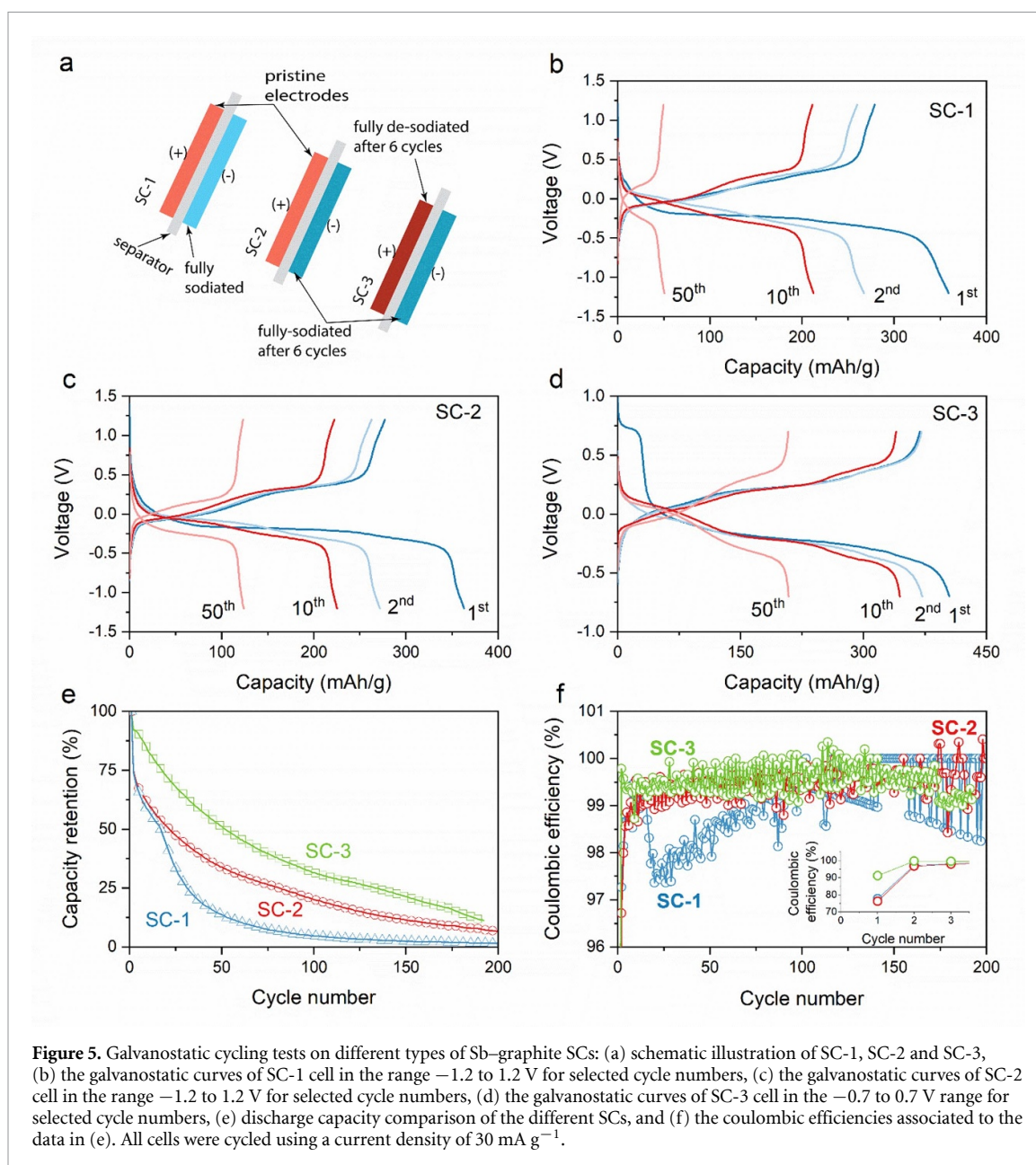
Figure 4. XPS spectra of pristine, soaked and Sb/graphite composite electrodes cycled in half-cells.

The C 1s and O 1s spectra of pristine and soaked samples display peaks originated from graphite and antimony oxide as well as from C–O, O–C=O species which are characteristic peaks of the sodium alginate binder present in the electrode [39, 40]. The peaks at 530 and 540 eV in O 1s correspond to Sb 3d<sub>5/2</sub> and Sb 3d<sub>3/2</sub>, respectively, of Sb–O, while the strong peak at 284.4 eV represent graphite in the electrode matrix [41]. However, these peaks originated from the electrode largely disappears when SEI forms after cycling. After five cycles, at sodiated state the graphite peak at 284.4 is almost invisible while it appears again at desodiated state. This indicates that SEI formed on graphite particles destroyed/removed during the desodiation.

The source of fluorine for the C–F species peak originates from degradation of NaPF<sub>6</sub> salt or FEC additive, thus the peak is not present in the pristine electrode. Two peaks can be observed in the F 1s spectra at about 685 eV and 688 eV originating from NaF and C–F species, respectively [42]. Peak shifts in the binding energy after cycling are attributed to differential charging effect of the cycled electrodes. The cycled electrodes in comparison with pristine and soaked electrodes generally show that SEI layer is formed after cycling, however SEI is unstable during the initial cycles (five cycles here) and thus becomes thinner during the desodiation. After 50 cycles however both desodiate and sodiated samples display almost similar SEI features and thickness.

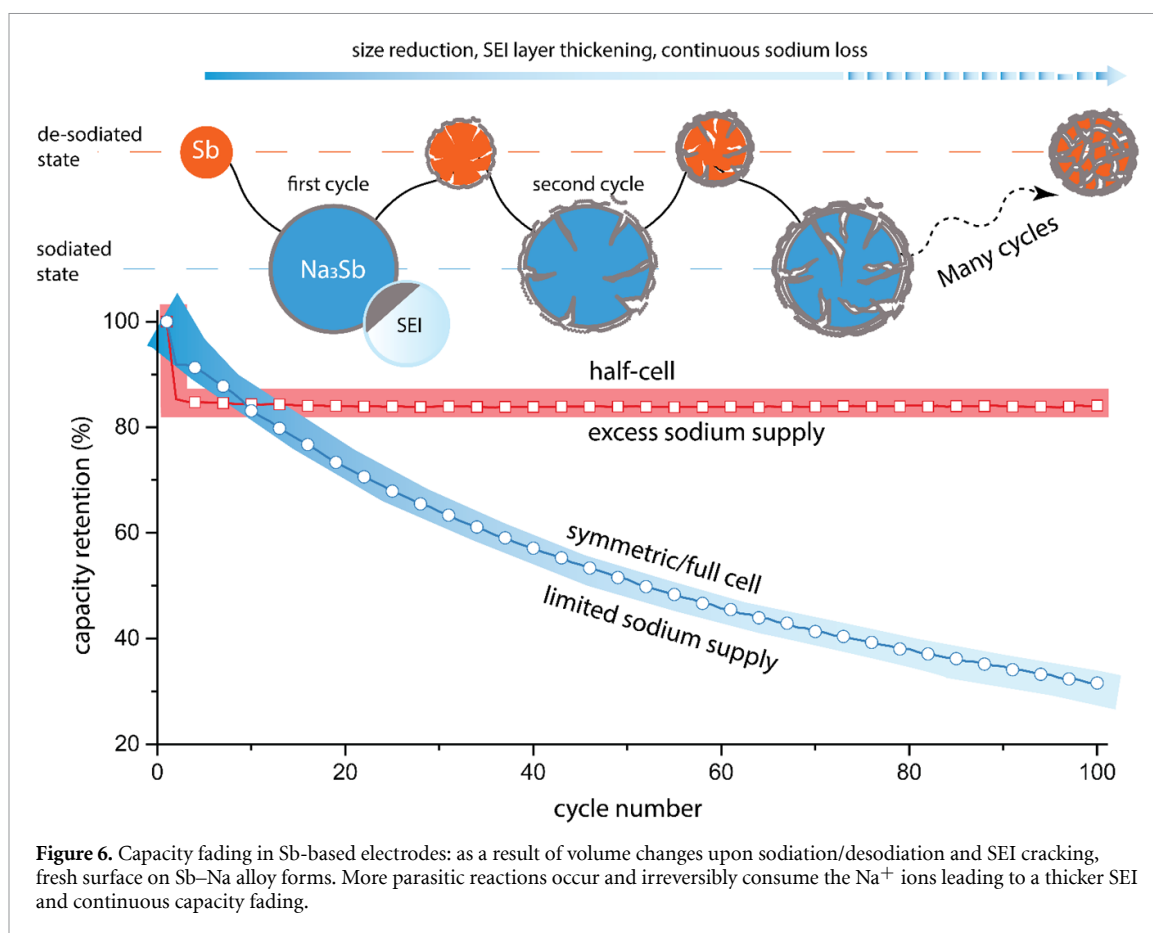
To further understand the interfacial stability, potential parasitic reactions, and capacity fading, SCs were investigated. Because of the limited amount of sodium ions available, contrary to half-cells in which the Na-metal counter electrode supplies sodium ions in excess, SCs are suitable to study the nature and stability of SEI layer and account for parasitic losses that lead to capacity fading over prolonged cycling [20, 43]. The SCs studied (figure 5(a)) in this work were assembled using two similar Sb–graphite electrodes, one charged and one discharged. A practical voltage interval was chosen for the galvanostatic measurements of the SCs in order to ensure a full sodiation/desodiation of each electrode.

The SC-1 cell (figure 5(a)) sustained a 22% capacity loss during the initial cycle attributed to electrolyte decomposition on the pristine composite electrode. To reveal if a stable SEI layer was fully formed during the first sodiation cycle, a symmetric cell SC-2 was assembled. The SC-2 (figure 5(a)) consisted of a Sb–graphite electrode that was pre-sodiated after six discharge–charge cycles and another Sb–graphite electrode without pre-sodiation steps. Similar to SC-1, a capacity loss of 24% was observed in the initial cycle due to electrolyte breakdown on the pristine electrode. The long-term cycling efficiency was, however, improved. The decrease



in capacity fade in SC-2 cell as compared to SC-1 cell confirmed the importance of more stable SEI in enabling better cycle life of Sb-based electrodes.

In SC-3 cell, both the negative and positive Sb-graphite electrodes were pre-cycled for at least six times prior to cell construction. As opposed to SC-1 and SC-2, the SC-3 showed initial CE above 90%, as both electrodes have been pre-sodiated to allow for the formation of SEI passivation that reduced electrolyte decomposition during the first few cycles. It also had a higher capacity retention over 200 cycles, as indicated in figure 5(e). Most importantly, the capacity fading in Sb-graphite electrodes in SCs was remarkably higher than in the half-cells. Significantly higher capacity retention was observed in half-cells in which the specific capacity suffered hardly any fading over 40 cycles, whereas in all of the SCs the capacity decreased continually as only limited amount of  $\text{Na}^+$ -ions were available for electrochemical reactions. This irreversible capacity could indicate that the SEI was somewhat continuously formed after every de-sodiation cycle. The SEI could be prone to damage as a result of volume changes during the alloying and dealloying reactions in which fresh reactive surfaces were forming, as illustrated in figure 6. The parasitic reactions on Sb-Na alloy involving the electrolyte could lead to irreversible consumption of sodium ions to form a continuously growing SEI. The excess availability of sodium ions from the sodium metal counter electrode in half-cells guarantees full sodiation of the electrode during every cycle. Therefore, the half-cell setups of Sb-graphite electrodes showed no capacity fading. Hence, it should be stressed that the actual performance of negative electrode materials must be tested in either full-cells or SCs.



#### 4. Conclusions

A composite Sb–graphite active material was prepared by ball-milling a mixture of Sb and graphite powders over 48 h. Structural analyses using, SEM, Raman spectroscopy and XRD confirmed the graphite and Sb particles underwent not only morphological but also structural changes as a result of mechanical milling. The composite electrode provided stable capacities between 350 and 400 mAh g<sup>-1</sup> at C/20, C/10 and C/5 with CE of about 80% which increased to above 98% from the second cycle onwards. Self-discharge tests of half-cells showed the capacity decreased by about 6% over 600 h, pointing to the presence of parasitic reaction occurring through the SEI layer. Different types of SCs, however, revealed that the capacity faded continuously because of continuous parasitic reactions which irreversibly consumed the Na<sup>+</sup> ions originating from the pre-sodiated Sb–graphite electrodes. Such reactions could involve the fresh surface on Sb–Na alloy forming as a result of the volume changes during cycling. The advantage of SCs over half-cells was clearly demonstrated as the electrode materials which displayed virtually no capacity loss in half-cell tests suffered from sharp capacity losses in the SCs wherein a limited amount of Na<sup>+</sup> ions was available. Therefore, it is necessary to use full-cells to truly characterize the performance of negative electrode materials, particularly those operating via alloying mechanism.

#### Data availability statement

All data that support the findings of this study are included within the article (and any supplementary files).

#### Acknowledgments

The authors acknowledge funding from the Swedish Strategic Research Program STandUp for Energy, and scientific assistance from Dr Ronnie Mogensen.

## ORCID iDs

Habtom Desta Asfaw  <https://orcid.org/0000-0001-5861-4281>

Reza Younesi  <https://orcid.org/0000-0003-2538-8104>

## References

- [1] Roberts S and Kendrick E 2018 The re-emergence of sodium ion batteries: testing, processing, and manufacturability *Nanotechnol. Sci. Appl.* **11** 23–33
- [2] Ge P and Foulletier M 1988 Electrochemical intercalation of sodium in graphite *Solid State Ion.* **28–30** 1172–5
- [3] Chevrier V L and Ceder G 2011 Challenges for Na-ion negative electrodes *J. Electrochem. Soc.* **158** A1011
- [4] Irisarri E, Ponrouch A and Palacin M R 2015 Review—hard carbon negative electrode materials for sodium-ion batteries *J. Electrochem. Soc.* **162** A2476–82
- [5] Carboni M, Manzi J, Armstrong A R, Billaud J, Brutti S and Younesi R 2019 Analysis of the solid electrolyte interphase on hard carbon electrodes in sodium-ion batteries *ChemElectroChem* **6** 1745–53
- [6] Asfaw H D, Tai C-W, Valvo M and Younesi R 2020 Facile synthesis of hard carbon microspheres from polyphenols for sodium-ion batteries: insight into local structure and interfacial kinetics *Mater. Today Energy* **18** 100505
- [7] Palomares V, Serras P, Villaluenga I, Hueso K B, Carretero-González J and Rojo T 2012 Na-ion batteries, recent advances and present challenges to become low cost energy storage systems *Energy Environ. Sci.* **5** 5884
- [8] He J, Wei Y, Zhai T and Li H 2018 Antimony-based materials as promising anodes for rechargeable lithium-ion and sodium-ion batteries *Mater. Chem. Front.* **2** 437–55
- [9] Lu X, Adkins E R, He Y, Zhong L, Luo L, Mao S X, Wang C M and Korgel B A 2016 Germanium as a sodium ion battery material: *in situ* TEM reveals fast sodiation kinetics with high capacity *Chem. Mater.* **28** 1236–42
- [10] Li Z, Ding J and Mitlin D 2015 Tin and tin compounds for sodium ion battery anodes: phase transformations and performance *Acc. Chem. Res.* **48** 1657–65
- [11] Zhou J, Dou Q, Zhang L, Wang Y, Yuan H, Chen J and Cao Y 2020 A novel and fast method to prepare a Cu-supported  $\alpha$ -Sb<sub>2</sub>S<sub>3</sub>@CuSbS<sub>2</sub> binder-free electrode for sodium-ion batteries *RSC Adv.* **10** 29567–74
- [12] Liang S, Cheng Y J, Zhu J, Xia Y and Müller-Buschbaum P 2020 A chronicle review of nonsilicon (Sn, Sb, Ge)-based lithium/sodium-ion battery alloying anodes *Small Methods* **4** 2000218
- [13] Mogensen R, Maibach J, Naylor A J and Younesi R 2018 Capacity fading mechanism of tin phosphide anodes in sodium-ion batteries *Dalton Trans.* **47** 10752–8
- [14] Zhu Y, Han X, Xu Y, Liu Y, Zheng S, Xu K, Hu L and Wang C 2013 Electrospun Sb/C fibers for a stable and fast sodium-ion battery anode *ACS Nano* **7** 6378–86
- [15] Li K, Su D, Liu H and Wang G 2015 Antimony-carbon-graphene fibrous composite as freestanding anode materials for sodium-ion batteries *Electrochim. Acta* **177** 304–9
- [16] Qian J, Chen Y, Wu L, Cao Y, Ai X and Yang H 2012 High capacity Na-storage and superior cyclability of nanocomposite Sb/C anode for Na-ion batteries *Chem. Commun.* **48** 7070–2
- [17] Zhao X, Vail S A, Lu Y, Song J, Pan W, Evans D R and Lee J J 2016 Antimony/graphitic carbon composite anode for high-performance sodium-ion batteries *ACS Appl. Mater. Interfaces* **8** 13871–8
- [18] He M, Kravchik K, Walter M and Kovalenko M V 2014 Monodisperse antimony nanocrystals for high-rate li-ion and na-ion battery anodes: nano versus bulk *Nano Lett.* **14** 1255–62
- [19] Liu C, Zeng F, Xu L, Liu S, Liu J, Ai X, Yang H and Cao Y 2020 Enhanced cycling stability of antimony anode by downsizing particle and combining carbon nanotube for high-performance sodium-ion batteries *J. Mater. Sci. Technol.* **55** 81–8
- [20] Burns J C, Krause L J, Le D-B, Jensen L D, Smith A J, Xiong D and Dahn J R 2011 Introducing symmetric Li-ion cells as a tool to study cell degradation mechanisms *J. Electrochem. Soc.* **158** A1417
- [21] Kang S-J, Park K, Park S-H and Lee H 2018 Unraveling the role of LiFSI electrolyte in the superior performance of graphite anodes for Li-ion batteries *Electrochim. Acta* **259** 949–54
- [22] Hatchard T D and Obrovac M N 2014 Evaluation of electrolyte salts and solvents for Na-ion batteries in symmetric cells *J. Electrochem. Soc.* **161** A1748–52
- [23] Ma L A, Naylor A J, Nyholm L and Younesi R 2021 Strategies for mitigating dissolution of solid electrolyte interphases in sodium-ion batteries *Angew. Chem., Int. Ed.* **60** 2–11
- [24] Disma F, Aymard L, Dupont L and Tarascon J-M 1996 Effect of mechanical grinding on the lithium intercalation process in graphites and soft carbons *J. Electrochem. Soc.* **143** 3959–72
- [25] Welham N J, Berbenni V and Chapman P G 2003 Effect of extended ball milling on graphite *J. Alloys Compd.* **349** 255–63
- [26] Zhu M, Kong X, Yang H, Zhu T, Liang S and Pan A 2018 One-dimensional coaxial Sb and carbon fibers with enhanced electrochemical performance for sodium-ion batteries *Appl. Surf. Sci.* **428** 448–54
- [27] Duan J, Zhang W, Wu C, Fan Q, Zhang W, Hu X and Huang Y 2015 Self-wrapped Sb/C nanocomposite as anode material for high-performance sodium-ion batteries *Nano Energy* **16** 479–87
- [28] Zhou X, Zhong Y, Yang M, Hu M, Wei J and Zhou Z 2014 Sb nanoparticles decorated N-rich carbon nanosheets as anode materials for sodium ion batteries with superior rate capability and long cycling stability *Chem. Commun.* **50** 12888–91
- [29] Wang Y, Alsmeyer D C and McCreery R L 1990 Raman spectroscopy of carbon materials: structural basis of observed spectra *Chem. Mater.* **2** 557–63
- [30] Ferrari A C and Robertson J 2000 Interpretation of Raman spectra of disordered and amorphous carbon *Phys. Rev. B* **61** 14095–107
- [31] Baggetto L, Hah H Y, Jumas J C, Johnson C E, Johnson J A, Keum J K, Bridges C A and Veith G M 2014 The reaction mechanism of SnSb and Sb thin film anodes for Na-ion batteries studied by x-ray diffraction, <sup>119</sup>Sn and <sup>121</sup>Sb Mössbauer spectroscopies *J. Power Sources* **267** 329–36
- [32] Ko Y N and Kang Y C 2014 Electrochemical properties of ultrafine Sb nanocrystals embedded in carbon microspheres for use as Na-ion battery anode materials *Chem. Commun.* **50** 12322–4
- [33] Wang G, Xiong X, Lin Z, Yang C, Lin Z and Liu M 2017 Sb/C composite as a high-performance anode for sodium ion batteries *Electrochim. Acta* **242** 159–64
- [34] Darwiche A et al 2018 The electrochemical sodiation of Sb investigated by operando x-ray absorption and <sup>121</sup>Sb Mössbauer spectroscopy: what does one really learn? *Batteries* **4** 25

- [35] Darwiche A, Marino C, Sougrati M T, Fraisse B, Stievano L and Monconduit L 2012 Better cycling performances of bulk Sb in Na-ion batteries compared to Li-ion systems: an unexpected electrochemical mechanism *J. Am. Chem. Soc.* **134** 20805–11
- [36] Ji L *et al* 2014 Controlling SEI formation on SnSb-porous carbon nanofibers for improved Na ion storage *Adv. Mater.* **26** 2901–8
- [37] Mogensen R, Colbin S and Younesi R 2021 An attempt to formulate non-carbonate electrolytes for sodium-ion batteries *Batteries Supercaps* **4** 1–25
- [38] Mogensen R, Brandell D and Younesi R 2016 Solubility of the solid electrolyte interphase (SEI) in sodium ion batteries *ACS Energy Lett.* **1** 1173–8
- [39] Bodenes L, Darwiche A, Monconduit L and Martinez H 2015 The solid electrolyte interphase a key parameter of the high performance of Sb in sodium-ion batteries: comparative x-ray photoelectron spectroscopy study of Sb/Na-ion and Sb/Li-ion batteries *J. Power Sources* **273** 14–24
- [40] Feng J, Wang L, Li D, Lu P, Hou F and Liang J 2018 Enhanced electrochemical stability of carbon-coated antimony nanoparticles with sodium alginate binder for sodium-ion batteries *Prog. Nat. Sci. Mater. Int.* **28** 205–11
- [41] Darwiche A, Bodenes L, Madec L, Monconduit L and Martinez H 2016 Impact of the salts and solvents on the SEI formation in Sb/Na batteries: an XPS analysis *Electrochim. Acta* **207** 284–92
- [42] Mogensen R, Maibach J, Brant W R, Brandell D and Younesi R 2017 Evolution of the solid electrolyte interphase on tin phosphide anodes in sodium ion batteries probed by hard x-ray photoelectron spectroscopy *Electrochim. Acta* **245** 696–704
- [43] Yan Z and Obrovac M N 2017 Electrolyte reactivity on graphite and copper as measured in lithium double half cells *J. Electrochem. Soc.* **164** A2977–86